Infrared Physics & Technology 152 (2026) 106247

Contents lists available at ScienceDirect

Infrared Physics and Technology

journal homepage: www.elsevier.com/locate/infrared

Research Paper

Synchrotron-based infrared microspectroscopy study on the biomolecular impact of carbon minibeam radiation therapy on a mouse osteosarcoma cell line☆

R. González-Vegas [a], M. Cots-Costa [a], C. Gilbert [b,c], A. Bertho [b,c], O. Seksek [d], C. Graeff [e], O. Sokol [e], W. Tinganelli [e], Y. Prezado [b,c,f,g,h], I. Yousef [i,*], I. Martínez-Rovira [a,*]

[a] Physics Department, Universitat Autònoma de Barcelona (UAB), 08193 Bellaterra, Cerdanyola del Vallès, Barcelona, Spain
[b] Institut Curie, CNRS UMR3347, Inserm U1021, Signalisation Radiobiologie et Cancer, Université PSL, 91400 Orsay, France
[c] CNRS UMR3347, Inserm U1021, Signalisation Radiobiologie et Cancer, Université Paris-Saclay, 91400, Orsay, France
[d] IJCLab, CNRS/IN2P3, Université Paris-Saclay, 91450 Orsay, France
[e] Biophysics Department, GSI Helmholtzzentrum für Schwerionenforschung, 64291, Darmstadt, Germany
[f] New Approaches in Radiotherapy Lab, Center for Research in Molecular Medicine and Chronic Diseases (CIMUS), Instituto de Investigación Sanitaria de Santiago de Compostela (IDIS), University of Santiago de Compostela, Santiago de Compostela, A Coruña, Spain
[g] Oportunius Program, Galician Agency of Innovation (GAIN), Xunta de Galicia, 15706 Santiago de Compostela, A Coruña, Spain
[h] Institut Curie Centre de Recherche, Rue Henri Becquerel, 91410, Orsay, France
[i] MIRAS Beamline BL01, ALBA-CELLS Synchrotron, 08209 Cerdanyola del Vallès, Barcelona, Spain

ARTICLE INFO

Dataset link: https://dataverse.csuc.cat/

Keywords:
Synchrotron-based Fourier transform infrared microspectroscopy
Minibeam radiation therapy
Carbon therapy
In vitro studies

ABSTRACT

Carbon minibeam radiation therapy (CMBRT) is a novel oncology treatment modality that combines the superior radiobiological properties of carbon ions with the remarkable tissue-sparing effects of spatial dose fractionation. Nevertheless, the differential biological mechanisms that CMBRT activates are not fully understood. To shed further light on such biomolecular processes, this study analysed the impact of CMBRT on LM8 osteosarcoma cells using synchrotron-based infrared microspectroscopy (SR-FTIRM). Samples were subjected to conventional carbon RT (CBB) and CMBRT at GSI (Germany). RT-treated cells underwent SR-FTIRM evaluations at ALBA Synchrotron (Spain) at 24 h post-RT. Principal component analysis (PCA) uncovered the main spectral differences between the treatment modalities, revealing that the IR signatures of CMBRT-treated samples were the most dissimilar from Control cells. Modifications of IR peaks attributed to α-helical and β-sheet protein sub-structures were consistent with the alterations of the Amide I spectral band due to CMBRT (assessed via curve-fitting analysis), suggesting enhanced protein oxidation. Conformational alterations in the sugar-phosphate backbone of nucleic acids might also have resulted from further oxidative damage due to CMBRT. Additionally, CMBRT led to greater alterations of methylene and methyl bands compared to CBB, which may have been caused by free radical attacks. Spectral signatures in the CMBRT valleys differed from those in the CMBRT peaks, suggesting distinct biomolecular mechanisms involved in these two dose regions. Comparison with proton and neon irradiations revealed common IR features affected by MBRT modalities.

1. Introduction

Cancer is one of the leading causes of death worldwide, with an estimated incidence of almost 30 million new cancer cases and over 15 million consequential deaths by the year 2040 [1]. The complexity of cancer usually requires a combination of different treatment modalities to improve the therapeutic outcome in patients. Surgery, chemotherapy and radiation therapy (RT) are the core standard techniques in oncology treatment. Notably, approximately 50% of cancer patients will receive at least one fraction of RT at some stage during the course of their treatment. RT has benefited over the last decades from a continuous technological progress, leading to improved treatment

☆ This article is part of a Special issue entitled: 'WIRMS 2024' published in Infrared Physics and Technology.

* Corresponding authors.
E-mail addresses: iyousef@cells.es (I. Yousef), Immaculada.Martinez@uab.cat (I. Martínez-Rovira).

https://doi.org/10.1016/j.infrared.2025.106247
Received 2 June 2025; Received in revised form 15 October 2025; Accepted 1 November 2025
Available online 5 November 2025

outcomes. Still, the care of some tumour types remains a major clinical challenge due to their inherent resistance to radiation. One example is osteosarcoma, the primary high-grade bone malignancy that is often fatal in children and young adults [2].

The standard treatment of osteosarcoma comprises the use of different chemotherapy regimens and surgical resection. The use of conventional RT for the management of osteosarcoma is limited, due to the increased resistance to radiation of this cancer variant. Still, the use of high-dose RT may help to achieve local control of osteosarcoma in patients in whom surgery is not possible [3]. However, the main hindrance to the use of high doses is the toxicity limitations imposed by healthy tissues surrounding the tumour. These tissues will inevitably receive unwanted radiation during RT; therefore, the quest for novel treatment strategies to overcome this constraint is of paramount importance. One approach that has recently received considerable attention is minibeam radiation therapy (MBRT) [4]. MBRT is a type of spatially fractionated RT (SFRT) in which a heterogeneous pattern of high-dose regions (peaks) separated by low-dose areas (valleys) is employed. The peaks are a set of parallel radiation beamlets 0.5–1.0 mm wide and spaced by a centre-to-centre (c-t-c) distance of 1–4 mm. This irradiation strategy has been shown to increase normal tissue dose tolerances using diverse beam types [5,6], while being at least as effective as conventional RT [7]. Recently, the first successful treatment of human patients with MBRT has proven the feasibility of this technique in a clinical scenario [8]. Regarding osteosarcoma, a previous study highlighted the use of MBRT in the treatment of this cancer type, suggesting a gain in normal tissue preservation while still using sufficiently high doses to achieve tumour control [9].

Given the promising characteristics offered by MBRT, a possible synergy could be achieved by combining this modality with heavy ion beams. The rationale underlying this combination lies in the superior radiobiological properties that these types of particles offer. In particular, carbon ions are generally considered the best particles in terms of physical and radiobiological features. Carbon beams show a steeper Bragg peak and reduced lateral scattering than X-rays or protons, resulting in higher dose conformity at the tumour position while reducing the toxicities to nearby normal tissues [10]. In addition, carbon ions exhibit a superior biological effectiveness and reduced oxygen enhancement ratio compared to other charged particle beams [11], which might enhance tumour eradication and even benefit the treatment of radiation-resistant malignancies.

Previous biological studies have highlighted the potential benefits of combining carbon ions with MBRT (CMBRT) [12]. A very recent study has analysed the differences in tumour growth delay in a murine model of osteosarcoma subjected to conventional (broad beam) carbon RT (CBB) and CMBRT. All irradiated animals received an average dose of 20 Gy in both treatment modalities and showed a significant and similar tumour growth delay compared to non-irradiated animals [13]. In the case of CMBRT, the authors noted that a significant fraction of the total tumour volume (about a 70%) received a valley dose as low as 1.5 Gy, suggesting that CMBRT triggered distinct biological mechanisms than CBB. This is a well-known fact, yet the complete picture of the fundamental principles that explain the healthy tissue-sparing effects and anti-tumour efficacy of MBRT is still lacking. Some of the mechanisms proposed to account for how normal and tumour tissues respond to MBRT are: the migration of stem cells from valley- to peak-irradiated healthy tissues to promote their repair [14]; the activation of an effective and rapid anti-tumour immune modulation [15]; a distinct vasculature impact, especially the pronounced effects on immature blood vessels [16]; triggering of intercellular signalling mechanisms, *i.e.* bystander/cohort and abscopal effects [17]; and the direct and indirect damage provoked by reactive oxygen species (ROS) [18].

One potential strategy to unravel some of the unresolved biomolecular mechanisms underlying MBRT would be to use synchrotron radiation-based Fourier transform infrared microspectroscopy (SR-FTIRM). This precise analytical tool employs infrared (IR) light to excite the vibrational state of molecular bonds present in the major biomolecules of cells (lipids, proteins, nucleic acids and carbohydrates). Thanks to the high-brilliance synchrotron light, the finely detailed IR spectra obtained with this technique allow comprehending the subtle biomolecular structure of the samples and reconstructing the action of the different RT modalities by assessing the spectral changes at a cellular level. SR-FTIRM has proven useful to analyse the biomolecular basis of novel RT approaches [19–25], including proton and neon MBRT [26,27].

In this context, the aim of this study is to unravel the biological mechanisms underlying CMBRT using SR-FTIRM. The effects of spatially fractionated carbon-ion beams on the IR spectral signatures of a mouse osteosarcoma cell line were compared with the biomolecular response to conventional carbon irradiations. In addition, the results of the present study were also compared with data on conventional RT and MBRT irradiations of various tumour cell lines using proton and neon-ion beams [26,27].

2. Materials and methods

2.1. Sample preparation & irradiations

LM8 (RRID:CVCL_6669) murine osteosarcoma cells, originating from C3H male mice [28], were prepared for irradiations following previous protocols [27]. Samples were cultured in high-glucose DMEM medium (Gibco™, LifeTechnologies SAS, Courtaboeuf, France) supplemented with 10% fetal calf serum, 1% penicillin-streptomycin (10 000 units/mL each), 1 mM GlutaMAX™, 1 mM sodium pyruvate and 10 mM HEPES. Incubation occurred in a chamber at 37 °C, 95% humidity and 5% CO_2. Cells were grown on 0.5 mm-thick CaF_2 coverglasses (Crystran Ltd), transparent to IR light. The coverglasses were edge-glued to one side of 12.5 cm^2 T-flasks (Falcon®, part no. 734-0010), into which a slightly smaller diameter hole had been drilled. In this way, cells were able to grow on the glass while retaining the volume of medium required for their growth. Moreover, by filling the flask with medium, it could be placed vertically to allow both horizontal irradiation and maintenance of cell life and proliferation (see Fig. 1). Each coverglass was seeded with 1 mL of cell suspension at a concentration of 1.25×10^4 cells/cm^2 to achieve a 75%–80% confluence rate on the day of irradiations.

The irradiations were performed at the fixed horizontal research station of Cave M at the GSI Helmholtz Centre for Heavy Ion Research (Darmstadt, Germany) [29]. ^{12}C-ion beams with an energy of 180 MeV/u (approximately 0.1% energy spread) were used for CBB and CMBRT irradiations. The spatial fractionation of the beam was achieved by using a multislit brass collimator ($70 \times 70 \times 30$ mm^3) with 15 vertical slits (0.5 mm wide and 50 mm high), spaced by a c-t-c distance of 3.6 mm. Fig. 1 shows a simplified schematic of the irradiation configuration for CMBRT. Samples were irradiated with two mean doses ($\overline{D}$) under CBB and CMBRT conditions: 2 Gy and 8 Gy. In the case of CMBRT, the peak-to-valley dose ratio (PVDR) was around 50, with peak and valley doses of (respectively) 9.8 ± 0.5 Gy and 0.18 ± 0.02 Gy (for $\overline{D} = 1.74 \pm 0.09$ Gy), and 44 ± 2 Gy and 0.85 ± 0.08 Gy (for $\overline{D} = 8.3 \pm 0.4$ Gy). Gafchromic™ EBT3 radiochromic films attached to the IR slides containing the samples allowed to guarantee irradiation quality, and to differentiate between CMBRT peak and valley dose regions (allowing the selection of the cells corresponding to these groups during SR-FTIRM measurements).

One day after irradiations, the medium of the flasks containing the samples was removed and slides were rinsed twice with phosphate-buffered saline (PBS). Then, samples were incubated for one hour at room temperature in 10% formalin neutral buffered solution (Sigma-Aldrich). Subsequently, three rounds of ultrapure Millipore water rinsing allowed washing out any residual phosphate ions in the slides [21,22]. Samples were finally dried out at room temperature for posterior SR-FTIRM analyses.

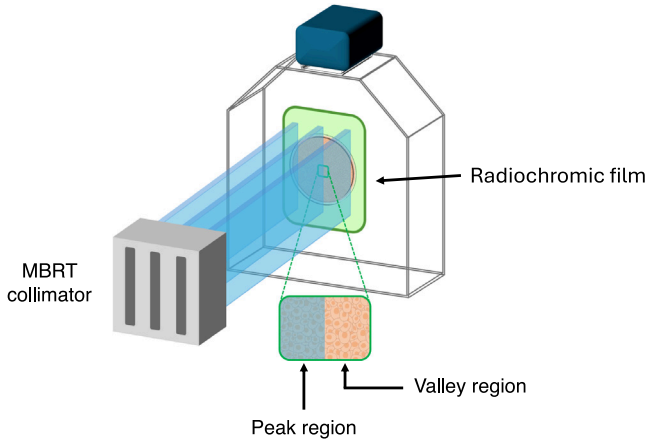

Fig. 1. Simplified schematic representation of the setup used for CMBRT irradiations. A multislit brass collimator generates the spatial fractionation of the carbon beam, which reaches the flask containing the cells. Different parts of the cell culture receive radiation from either the peak or valley regions of spatially fractionated carbon beams. A radiochromic film, sensitive to radiation, is attached to the back of the flask for posterior dosimetry verification, as well as to allow the selection of cells in the peak and valley regions of CMBRT.

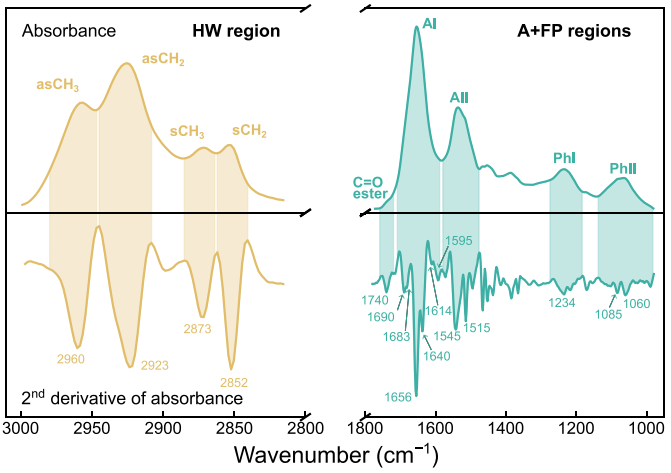

Fig. 2. Representative IR absorbance spectrum (top) of a cell and its second derivative (bottom) in the HW (left, yellow) and A+FP (right, green) spectral regions. Coloured areas represent the ranges of the most prominent IR bands in both spectral regions (labelled in the absorbance spectrum, top). Second-order differentiation enables the resolution of overlapping sub-peaks in the raw absorbance spectrum; the position (in cm^{-1}) of the most relevant sub-peaks are indicated (bottom). The absorbance spectrum was baseline corrected and vector normalised; second-order differentiation of the spectrum was performed by applying the Savitzky–Golay filter, followed by vector normalisation.

2.2. SR-FTIRM at ALBA synchrotron

Irradiated LM8 samples were submitted to SR-FTIRM measurements at the MIRAS beamline of ALBA-CELLS Synchrotron (Cerdanyola del Vallès, Spain). The end-station allows IR spectra acquisition with the Hyperion 3000 microscope coupled to the Vertex 70 spectrometer (Bruker Optics GmbH, Germany) using a mercury cadmium telluride liquid nitrogen-cooled detector. Around 100 cells were individually selected from each sample configuration (Control, BB, MB_{peak}, MB_{valley}). The IR beam size was set to $12 \times 12\,\mu m^2$. The transmission operation mode of the microscope was employed to collect cellular spectra in the 4000–900 cm^{-1} mid-IR spectral range. 256 co-added scans were recorded per spectrum with a spectral resolution of 4 cm^{-1}. Background spectra were also collected every 5 measurements in a sample-free region with the same number of co-added scans as mentioned above; this allowed to correct for varying ambient conditions in the beamline (CO_2 and water vapour levels) during the experiment.

2.3. Data analysis

Analysis of the IR data was carried out with the Quasar software (version 1.11.1) [30]. Principal component analysis (PCA) was employed as a dimensionality reduction method to assess the differences in spectral signatures according to the RT modality. The analysis was conducted in the 3000–980 cm^{-1} spectral range; PCA was applied to two separate spectral regions, shown in Fig. 2: the higher wavenumber region (HW; 3000–2815 cm^{-1}), originating from C-H stretching modes of the hydrocarbon chains of membrane lipids [31]; and the amides + fingerprint regions (A+FP; 1800–980 cm^{-1}), primarily originating from C=O stretching, C–N stretching, and N–H bending modes of the amide groups present in proteins and peptides (1800–1480 cm^{-1}) [32], and from a series of complex sugar-phosphate vibrations of the nucleic acids and carbohydrates (1350–980 cm^{-1}) [33]. PCA was conducted on second-derivative IR spectra: a Savitzky–Golay filter (second derivative order; 11 points window for the HW region, 21 points window for the A+FP regions) and unit vector normalisation were applied to IR data before PCA.

A curve-fitting analysis of the Amide I (AI, 1715–1585 cm^{-1}) spectral band was also conducted, allowing to assess the relative contribution of sub-bands attributed to various protein sub-structures. Following previous studies [30,34,35], a linear baseline correction was applied to the AI spectral range. Six Gaussian bands were fitted, the positions of which were identified by second-order differentiation of the AI band: intermolecular β-structure (1703–1687 cm^{-1}), intramolecular β-structure (1693–1669 cm^{-1}), α-helix (1671–1641 cm^{-1}), β-sheet + unordered structure (1648–1627 cm^{-1}), intermolecular β-structure (1636–1610 cm^{-1}), and side chain (1607–1592 cm^{-1}) [32,36]. It should be noted that, due to their proximity, the assignment of the bands attributed to β-sheet (centred near 1630 cm^{-1}) or to unordered (centred near 1640 cm^{-1}) structures could be equivocal [34,37]. In this study, only one peak near 1636 cm^{-1} was fitted, which was attributed to both contributions and labelled as βU. Similarly, some authors detected a splitting of the band associated with intramolecular β-structures (1693–1669 cm^{-1}), linking the two resulting bands with parallel β-sheets (centred near 1678 cm^{-1}) and β-turns (centred near 1666 cm^{-1}) [38]. Fig. 3 shows an example of the curve-fitting analysis of the AI band, indicating each of the previously mentioned sub-bands. The starting positions of the six Gaussian bands to fit were let to vary 2–10 cm^{-1}, and the full width at half maximum (FWHM) by 5–30 cm^{-1} [35]. All spectra of Control and irradiated configurations were subjected to the curve-fitting analysis; additionally, fits of the average AI band for each configuration were also obtained for easier visualisation of the results.

In order to elicit further biomolecular modifications due to RT treatments, ratios of the total areas of specific spectral bands were analysed:

- Amide I (1715–1585 cm^{-1}) to Amide II (1574–1481 cm^{-1}), AI/AII;
- Phosphate I (1275–1182 cm^{-1}) to Amide II (1574–1481 cm^{-1}), PhI/AII;
- Phosphate II (1139–982 cm^{-1}) to Amide II (1574–1481 cm^{-1}), PhII/AII;
- Asymmetric methylene (2947–2906 cm^{-1}) to asymmetric methyl (2981–2947 cm^{-1}), $asCH_2/asCH_3$;
- Carbonyl ester (1760–1723 cm^{-1}) to asymmetric methyl (2981–2947 cm^{-1}), C=O/$asCH_3$.

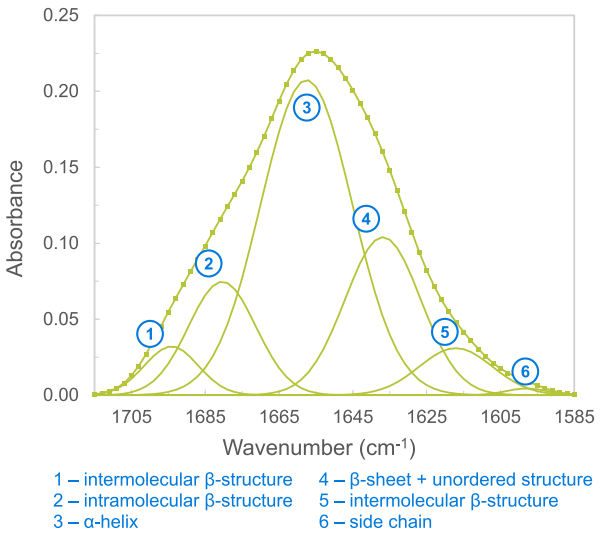

Fig. 3. Example of a curve-fitting analysis of the AI band. Each sub-band, corresponding to the continuous green curves of the fit, is associated to one of the six Gaussian functions attributed to the different protein secondary structures indicated in the lower part of the figure. The AI fit, resulting from the sum of each individual sub-band, is indicated by the continuous green curve with square markers.

Integration of each IR band was performed on baseline-corrected raw spectra using a rubber-band algorithm. In addition, the ratio between areas of the spectral bands attributed to β-sheet + unordered structures and of the α-helix structures (βU/α) was also assessed after the curve-fitting analysis of the AI band. Statistical analysis of the ratios was conducted with the software R (version 4.3.2) [39]. Global differences between RT modalities were assessed with a Kruskal–Wallis test and, if statistically significant, a Dunn test with the Bonferroni correction was applied for pairwise comparisons between RT modalities.

Additionally, the results of the present study were compared with our data on conventional RT and MBRT treatment of various tumour cell lines using proton beams (pBB and pMBRT, respectively; F98 rat glioma cell line) [26] and neon-ion beams (NeBB and NeMBRT, respectively; B16-F10 mouse melanoma cell line) [27]. The following mean (physical) doses were compared: 20 Gy for protons, 8 Gy for carbon ions, and 8 Gy for neon ions. For each study, samples were fixated 24 h post-irradiations; further details on sample preparation and irradiations with proton and neon-ion beams can be found in the corresponding publications. [26,27].

3. Results and discussion

Section 3.1 includes the results of the PCA analysis in the A+FP spectral regions, as well as the curve-fitting analysis of the AI band. The probability density assessment of the spectral band ratios is also included, followed by Section 3.2 devoted to the PCA in the HW spectral region. Lastly, Section 3.3 includes the comparison of the data of the present study with our data on proton and neon irradiations.

3.1. Amides + fingerprint regions

Fig. 4 shows the PCA results in the A+FP regions for the LM8 samples. Principal component (PC) scatter plots delineate the grouping of clusters according to the spectral differences between treatment modalities; the loading plots indicate the most relevant spectral features (wavenumbers) that contribute to data separation. Most of the separation between RT modalities occurs along the PC1 axis. For the two doses, both MB_{peak} and MB_{valley} groups are segregated from Control. The CBB group remains closer to the non-irradiated sample than CMBRT groups for both studied doses, especially for 2 Gy. Differences between CMBRT peak and valley regions are only seen for 2 Gy, with the latter group being the most differentiated from Control cells. The loadings revealed that the main spectral features contributing to group segregation were encountered in the AI spectral range (1715–1585 cm^{-1}), indicative of different protein secondary structures. In particular, the peak near 1666 cm^{-1} is associated with vibrational modes of α-helical geometries [32,38], whereas the peaks at 1635 cm^{-1} and 1631 cm^{-1} originate predominantly from β-sheet sub-structures, but may also include contributions from unordered structures [37]. The loadings revealed that the negative score of the peak attributed to the α-helix sub-band is associated with the delineation of Control and CBB groups, whereas the positive score of the β-sheet peak is associated with the separation of CMBRT-treated cells from Control and CBB clusters. Further details on the modifications induced by the irradiation modalities on the secondary structure of proteins by means of curve-fitting analysis of the AI band are given later in this section. Peaks in the spectral range of the AII band (1574–1481 cm^{-1}) also contributed to data separation. In particular, modifications of IR signatures associated with α-helices (peak near 1555 cm^{-1}) and β-sheets (peak near 1510 cm^{-1}) contributed most to group segregation. Again, the peak attributed to α-helical geometries is associated with the separation of Control and CBB groups, whereas the IR band attributed to β-sheet sub-structures contributed greatly to the segregation of MB_{peak} and MB_{valley} groups. For 8 Gy, separation of the CBB group from the Control sample is also associated with modifications of the β-sheet peaks of AI and AII bands. Lastly, the peak near 1468 cm^{-1} also contributed to data segregation. This peak originates from vibrational modes of lipid-related groups. Therefore, its discussion is included in Section 3.2 dedicated to the HW spectral region.

Alterations of the amide bands are considered indicative of conformational modifications in the secondary structure of proteins [32]. Through the PCA, one can notice that these alterations are primarily related to the effects of CMBRT. Previous works suggested these modifications to originate from oxidation mechanisms of existing proteins and amino acid chains, alterations of their conformational stability or aggregation of new proteins [40]. The trend of the AI/AII spectral ratio, which has been previously correlated with modifications in the secondary structure of proteins [41], was also inspected. Fig. 5 (first column) shows that irradiated groups have lower values of the ratio than the Control sample, especially the MB_{peak} and MB_{valley} groups. The observed changes in this ratio are consistent with the PCA results, showing that the most important alterations in the secondary structure of proteins are associated with the effects of CMBRT; these changes might also be indicative of alterations in DNA repair processes, since the main enzymes involved in nucleic acid repair mechanisms are proteins [19]. Additionally, modifications of the AI and AII bands were detected as signatures of different cell death mechanisms, which could affect the overall folding and localization of proteins and consequently the IR absorption of peptide bonds [42,43].

In order to investigate further alterations of protein secondary structures according to the RT modalities, a curve-fitting analysis of the AI band was conducted. The entire data set for each irradiation configuration was subjected to this analysis and the discussion is based on the results for all spectra; nonetheless, for visualisation purposes, the upper panel of Fig. 6 includes the fits of the average AI spectral band of Control and irradiated samples, showing the several sub-bands mentioned in Section 2.3 that conform the whole AI spectral range. The main modifications occurred in the sub-bands attributed to α-helix and βU secondary structures: a slight decrease in the amplitude of the former band (1671–1641 cm^{-1}, centred near 1656 cm^{-1}) and an amplitude increase for the latter (1648–1627 cm^{-1}, centred near 1636 cm^{-1}) for MB_{peak} and MB_{valley} groups were observed for both doses. These alterations resulted in a statistically significant increase of the βU/α ratio for CMBRT-treated samples with respect to Control and CBB groups (lower panel of Fig. 6); for 8 Gy, no statistically

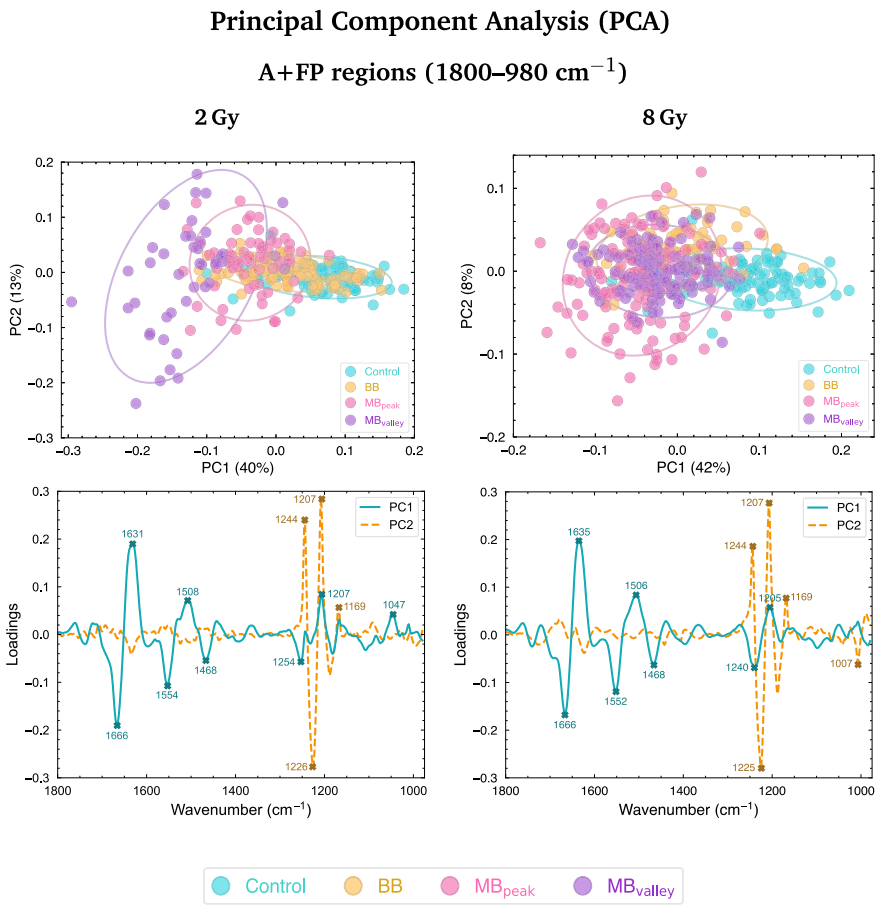

Fig. 4. PCA in the A+FP (1800–980 cm^{-1}) spectral regions of LM8 mouse osteosarcoma cells irradiated with 2 Gy or 8 Gy carbon beams. For each spectral region, the PC scatter plots (upper row) and loadings (lower row) are included. Each point on the PC scatter plots represents a cell spectrum, and colours correspond to the irradiation configurations: blue for Control (non-irradiated), orange for BB, pink for MB$_{peak}$ and purple for MB$_{valley}$. 95% confidence ellipses are included, and explained variances by the PCs are shown in parentheses. In the loadings, the contribution of each spectral band to data separation along PC1 is indicated by solid blue lines, while the bands contributing to the separation along PC2 are indicated by dashed orange lines. The most relevant IR peaks contributing to cluster delineation along PC1 or PC2 are marked with blue or orange labels and crosses, respectively. Indicated doses refer to the mean dose for both CBB and CMBRT modalities.

significant differences between BB and MB$_{peak}$ groups were detected. These modifications are consistent with the results of the PCA, and reflect a significant degree of structural alterations in the proteins, mainly due to CMBRT. These spectral changes could be the result of protein peroxidation: the generation of hydroperoxyl radicals (which lead to fragmentation of the protein backbone) and the addition of carbonyl moieties to amino acid side chains due to exposure to ionising radiation may have affected the absorption of the C=O bonds present in the AI [44], and thus induce the alterations observed in the α-helix and β-sheet spectral bands. Lipid auto-oxidation products might have also modified the secondary structure of proteins and resulted in the transitions from α-helical to β-sheet geometries [45]. The alterations of the above-mentioned protein spectral signatures have also been previously ascribed to a redistribution or denaturation of proteins following cell death mechanisms [42,46]. In particular, transitions from α-helical geometries to β-sheets or unordered structures in proteins were detected in apoptotic and necrotic cells [43,47]. Other authors reported that histones, which are molecules involved in DNA damage repair pathways, undergo modifications in their secondary structure after exposure to radiation. Specifically, an increase in β-sheet and unordered structures along with a concomitant decrease in α-helix content was observed in H3–H4 histones after X-ray irradiations [48]. Regarding the rest of sub-bands, mild modifications were observed, but no clear trends could be identified for the different irradiation configurations or doses.

The lower frequency region also contributes to the segregation of the RT modalities for the two doses after the PCA. The peaks close to 1254 cm^{-1} (2 Gy) and 1240 cm^{-1} (8 Gy) in the loadings of Fig. 4 are part of the PhI band and arise from asymmetric stretching vibrations of PO_2^- moieties of the phosphodiester bonds forming the sugar-phosphate backbone of DNA and RNA [33]. In particular, these peaks are part of the main spectral marker of A-form DNA (1255–1235 cm^{-1}) [33], and are associated with the separation of Control and CBB clusters from CMBRT-treated groups; for the highest dose, spectral modifications of these peaks allowed to differentiate Control from CBB-treated samples as well. Modifications of these peaks for the MB$_{peak}$ and MB$_{valley}$ groups may result from conformational changes in the DNA or even cell cycle alterations induced by irradiations [19]. The peaks at 1207 cm^{-1} (2 Gy) and 1205 cm^{-1} (8 Gy) arise from PO_2^- stretching vibrations of Z-form helices of the DNA [33], and are associated with the segregation of CMBRT groups from Control and CBB clusters, especially of the MB$_{valley}$ group for 2 Gy. Alterations of this band may arise from cleavage or damage to the double-helix structure of the DNA [49]. Additionally, for the lowest dose, a band at 1047 cm^{-1} did also contribute to data segregation; this peak is one of the main vibrational modes constituting the PhII band and is assigned to C–O stretching of the nucleic acids backbone and furanose [33], and is linked to the segregation of CMBRT groups from non-irradiated and CBB-treated samples. Irradiation-induced alterations of the above-mentioned spectral bands might be informative of DNA and/or RNA backbone conformations and

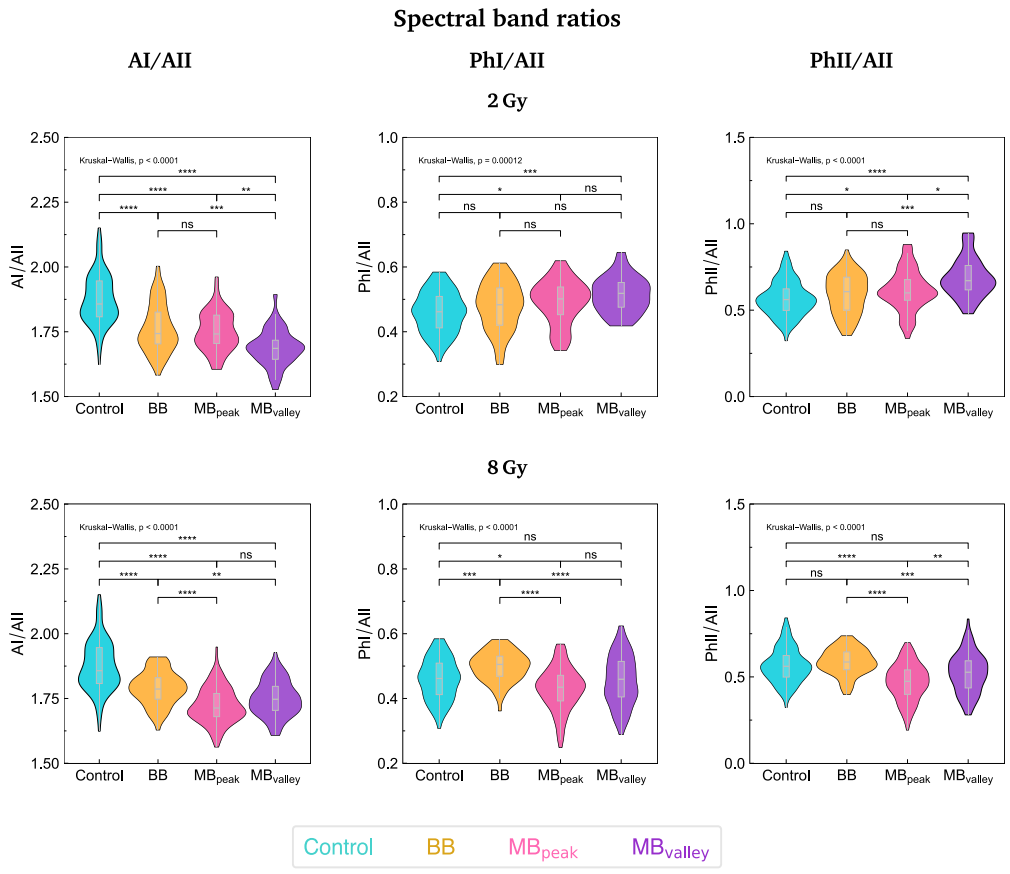

Fig. 5. Violin plots showing the probability density distribution of the AI/AII (first column), PhI/AII (second column) and PhII/AII (third column) spectral band ratios for LM8 mouse osteosarcoma cells irradiated with 2 Gy (upper row) or 8 Gy (lower row) carbon beams. Colours correspond to the irradiation configurations: blue for Control (non-irradiated), orange for BB, pink for MB_{peak} and purple for MB_{valley}. *p*-value significance levels are indicated as: ns ($p > 0.05$), * ($p \leq 0.05$), ** ($p \leq 0.01$), *** ($p \leq 0.001$), **** ($p \leq 0.0001$).

cleavage [49], DNA degradation or condensation [50], nucleotide base alterations in the RNA [51] or oxidative stress [52].

In addition, PC2 loadings point to a great contribution from the 1250–1150 cm^{-1} spectral range, albeit mainly related to intra-group variability of the CMBRT data. A slight separation between CBB-irradiated cells from Control and CMBRT-treated samples can be observed along the PC2 axis for 8 Gy as well. In addition to the peaks at 1244 cm^{-1} and 1207 cm^{-1} discussed in the previous paragraph, two additional contributions are identified in the loadings: the peak near 1225 cm^{-1}, corresponding to the PhI band and considered the main marker of B-form DNA [33], and the peak close to 1169 cm^{-1}, arising from –C–OH and C–O stretching modes of the DNA and RNA [43,53]. Alterations of these IR features also indicate conformational changes in the nucleic acid structures or modifications of the helices of nucleic acids due to the effects of CMBRT [33].

The behaviour of the PhI/AII and PhII/AII spectral ratios was also inspected (Fig. 5, second and third columns, respectively). Changes in these markers are considered indicators of radiation-induced modifications in nucleic acids and carbohydrates [43]. For each dose, the two ratios follow similar trends. On the one hand, in 2 Gy irradiations, an increase in the values for CMBRT-treated samples (especially for the MB_{valley} group) compared to Control is observed. A previous study analysed the DNA damage to an *in vitro* model of prostate adenocarcinoma (PC-3 cell line) upon proton irradiations [51]; the authors observed an intensity increase of PhI and PhII bands one day after irradiations, which may have resulted from enhanced DNA breakages or DNA denaturation [54,55]. Increased values of these ratios were also ascribed to the effects of cells being under oxidative stress conditions [52]. On the other hand, a reduction of the ratios for CMBRT groups can be seen for 8 Gy irradiations (especially for the MB_{peak} group). Some researchers observed an absorbance reduction of PhI and PhII bands on apoptotic cells [41,50]. These reductions are also suggestive of strand cleavage processes and chromatin fragmentation due to an increased number of double strand breaks [54]. Interestingly, CBB-treated cells show a significant increase in their values with respect to non-irradiated cells for the PhI/AII ratio.

As already highlighted in the preceding paragraphs, PCA and curve-fitting analysis revealed a different biomolecular response of samples to the MB_{peak} and MB_{valley} groups for the lowest dose. Some authors previously observed this hypersensitivity to low doses in a variety of cell lines, and proposed that a dose threshold of approximately 0.30 Gy is necessary to activate the different DNA repair pathways [56]. In the present study, the actual dose received by samples exposed to the MBRT valleys in 2 Gy (mean dose) irradiations was 0.18 ± 0.02 Gy, below such threshold. The possible unrepaired DNA lesions due to low-dose exposure may have led to the differential spectral modifications observed in the MB_{valley} group. This may also explain the minimal differences between the MBRT peak and valley clusters at 8 Gy: the MB_{valley} group received 0.85 ± 0.05 Gy, well above the 0.30 Gy threshold. Other plausible explanations for the observed spectral modifications associated with the MB_{valley} group may be due to structural alterations of amino acid chains, changes in protein stability, binding or folding, or aggregation of proteins following irradiations [40,57]. Changes in protein stability or phosphorylation processes might also be correlated with the expression of proteins involved in protein folding and stress response [58,59]. Additionally, several authors have investigated cell signalling mechanisms (*i.e.* bystander or abscopal effects) with FTIRM. Modifications of spectral signatures associated with C–O vibrations of

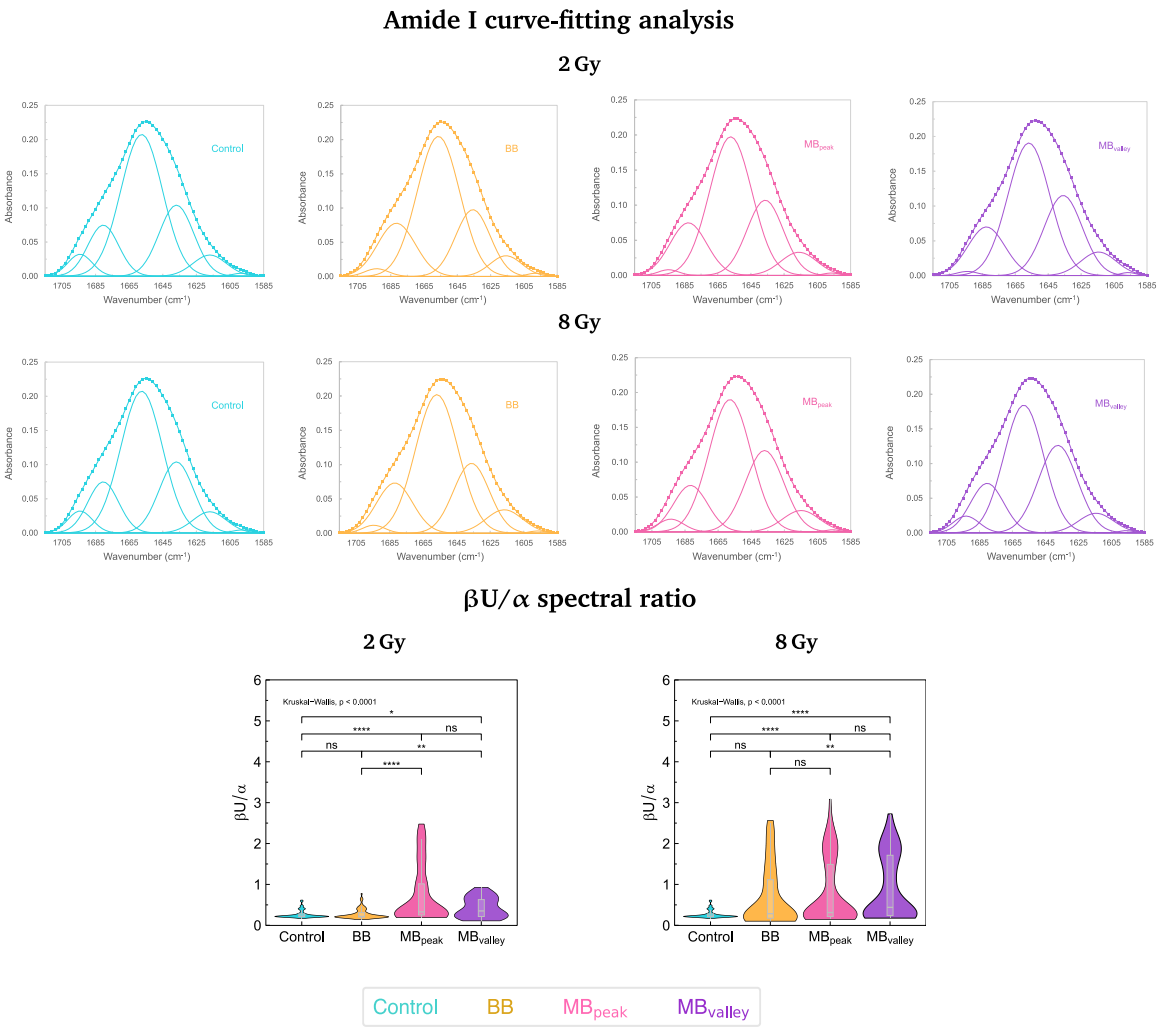

Fig. 6. Upper panel: curve-fitting analysis of the average AI spectral band for LM8 mouse osteosarcoma cells irradiated with 2 Gy (top) or 8 Gy (bottom) carbon beams. Each column and colours correspond to the irradiation configurations: blue for Control (non-irradiated; first column), orange for BB (second column), pink for MB_{peak} (third column) and purple for MB_{valley} (fourth column). Each sub-band, corresponding to the continuous lines of the fits, is associated to one of the 6 Gaussian functions attributed to the different protein secondary structures mentioned in Section 2.3. The AI fit, resulting from the sum of each individual sub-band, is indicated by the continuous curves and square markers. Lower panel: violin plots showing the probability density distribution of the βU/α spectral band ratio for LM8 mouse osteosarcoma cells irradiated with 2 Gy (left) or 8 Gy (right). Colours correspond to the irradiation configurations: blue for Control (non-irradiated), orange for BB, pink for MB_{peak} and purple for MB_{valley}. *p*-value significance levels are indicated as: ns ($p > 0.05$), * ($p \leq 0.05$), ** ($p \leq 0.01$), *** ($p \leq 0.001$), **** ($p \leq 0.0001$).

the nucleic acids, β-sheets and α-helices were ascribed to the indirect cell signalling effects and other cell death processes [60–62]; these structural alterations were similar to the ones contributing to differentiate the MB_{valley} group in the present study, and may be related to such biological processes.

3.2. Higher wavenumber region

Fig. 7 shows the PCA in the HW region. The effects of CMBRT treatment resulted in both MB_{peak} and MB_{valley} clusters clearly separated from Control and CBB groups. Regarding conventionally-treated cells, there were no differences between their IR signatures compared to the non-irradiated sample for the lowest dose; for 8 Gy, the CBB-treated group became differentiated from the Control cluster, but remained closer to the non-irradiated sample than cells subjected to CMBRT. Again, the PC1 axis accounts for most of the segregation of irradiation modalities. The four main bands present in the HW region arise from the methyl asymmetric (2981–2947 cm^{-1}, $asCH_3$) and symmetric (2884–2864 cm^{-1}, sCH_3) stretching modes, and the methylene asymmetric (2947–2906 cm^{-1}, $asCH_2$) and symmetric (2863–2840 cm^{-1}, sCH_2) stretching vibrations [31]. The loadings revealed that both methyl vibrational modes, as well as the $asCH_2$ band, are associated with the separation of CMBRT-treated cells, whereas the methylene bands are the ones accounting for the delineation of Control and CBB groups; this suggests that CMBRT induced conformational changes in these bands, resulting in the observed spectral differences compared to Control and CBB-treated samples. Separation between MB_{peak} and MB_{valley} groups is only noticeable for 2 Gy irradiations. In particular, a great intra-group variability of the MB_{valley} cluster for 2 Gy irradiations arises primarily from alterations of the $asCH_2$ band. Additionally, the contribution of the peak near 1468 cm^{-1} in the A+FP spectral region arises from CH_2 bending modes of cellular phospholipids. This band also contributes to the segregation of Control and CBB groups from CMBRT clusters. Modifications of this spectral band might be related to conformational changes in the phospholipid membranes of cells [40].

An inspection of the $asCH_2/asCH_3$ spectral ratio (Fig. 8, first column) reveals a similar trend for both doses: a reduction of the values for CMBRT groups can be seen compared to Control, especially for the MB_{valley} group in 2 Gy irradiations. A reduction of the ratio for the CBB modality can also be seen for 8 Gy. As suggested by the results of

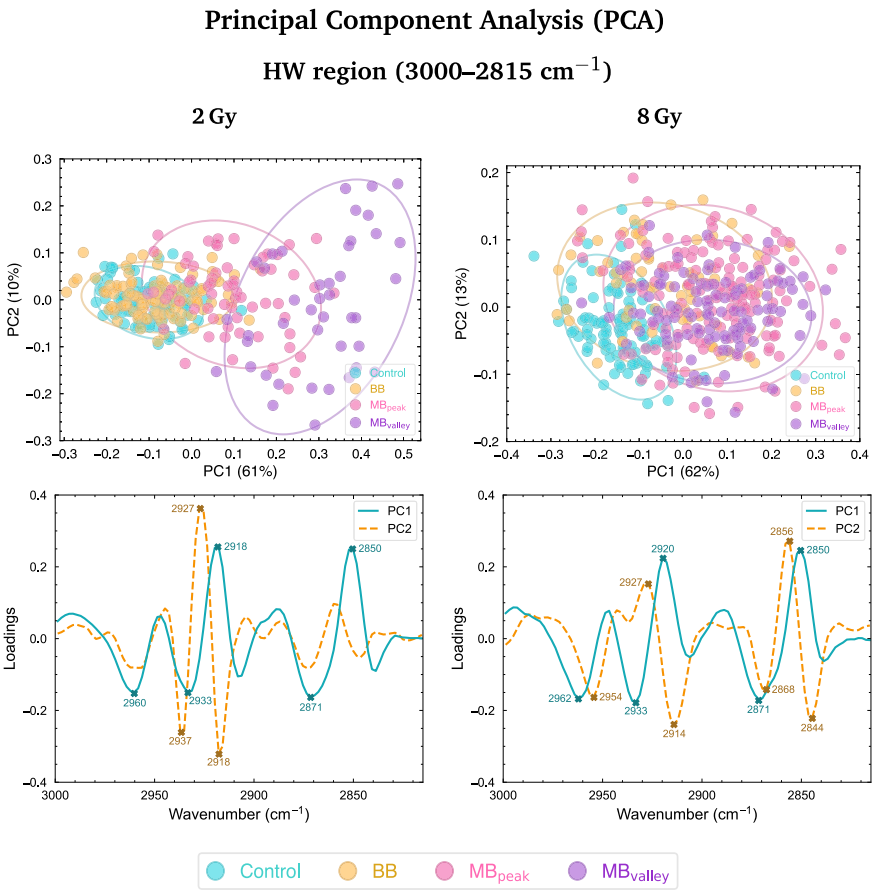

Fig. 7. PCA in the HW (3000–2815 cm^{-1}) spectral regions of LM8 mouse osteosarcoma cells irradiated with 2 Gy or 8 Gy carbon beams. For each spectral region, the PC scatter plots (upper row) and loadings (lower row) are included. Each point on the PC scatter plots represents a cell spectrum, and colours correspond to the irradiation configurations: blue for Control (non-irradiated), orange for BB, pink for MB_{peak} and purple for MB_{valley}. 95% confidence ellipses are included, and explained variances by the PCs are shown in parentheses. In the loadings, the contribution of each spectral band to data separation along PC1 is indicated by solid blue lines, while the bands contributing to the separation along PC2 are indicated by dashed orange lines. The most relevant IR peaks contributing to cluster delineation along PC1 or PC2 are marked with blue or orange labels and crosses, respectively. Indicated doses refer to the mean dose for both CBB and CMBRT modalities.

the PCA, this behaviour originates from the enhanced modifications of the C-H vibrational modes in CMBRT-exposed samples. These spectral alterations of the C-H vibrational modes are often ascribed to cells being subjected to free radical attacks, altering the saturation of acyl chains and phospholipid membranes [63]. The observed differences in lipid-related spectral bands between the peak and valley regions of CMBRT, particularly for the low dose, might be explained by a previous work that assessed the primary yields of different free radical species and ROS during water radiolysis [64]: reduced primary yields of hydrogen peroxide (H_2O_2) and increased primary yields of hydroxyl radicals ($^{\cdot}OH$) and aqueous electrons (e^-_{aq}) in the valleys compared to the peaks were observed for CMBRT. The authors attributed this behaviour to the increased linear energy transfer (LET) of carbon beams and the large proportion of nuclear fragments present in the valley regions, which would induce a different set of pre-chemical processes and chemical reactions than in the peak regions, leading to an increased level of indirect DNA damage in the low-dose regions of CMBRT. In addition, H_2O_2 is considered a good candidate to explain the tumour control efficacy of MBRT [18], and might also be involved in the non-targeted effects and the immune response activation observed in MBRT [13]. Free radicals and ROS can cause degradation of both the structure and function of lipids [65], which may have resulted in the methyl and methylene spectral alterations observed in this study. Other authors correlated the reduction of the $asCH_2/asCH_3$ spectral ratio with lipid peroxidation. Nonetheless, previous studies reported that this process is often accompanied by an increase in the absorbance of the C=O carbonyl ester band [66] (to be discussed later in this section) and an intensity decrease of the C-H stretching modes of unsaturated fatty acids (~3010 cm^{-1}) [65]. In the present study, apart from the reduction in the $asCH_2/asCH_3$ spectral ratio, neither of the alterations for the carbonyl ester and unsaturated fatty acids spectral bands were detected.

Another relevant spectral band related to the total lipid content of cells is the carbonyl ester band near 1740 cm^{-1} (found in the A+FP regions), which arises from C=O vibration modes of alkyl chains [42]. In particular, the $C{=}O/asCH_3$ ratio was examined (Fig. 8, second column). A reduction in the values of the ratio for CMBRT groups compared to Control can be seen, especially for 8 Gy. Some authors reported that the C=O carbonyl ester band was no longer detectable after low-dose X-ray exposure, suggesting an increased susceptibility to breakage of this bond following irradiations [67]. In addition, modifications of the C=O ester groups were reported in the IR spectra of dying cells, ascribing these effects to oxidative damage processes [42]. Other authors ascribed to modifications of the C=O ester to alterations of the nucleic acid base residues or to conformational changes due to oxidation processes of these base residues, implying stability alterations or even breakages in the hydrogen bonds between the nucleic acid bases [40].

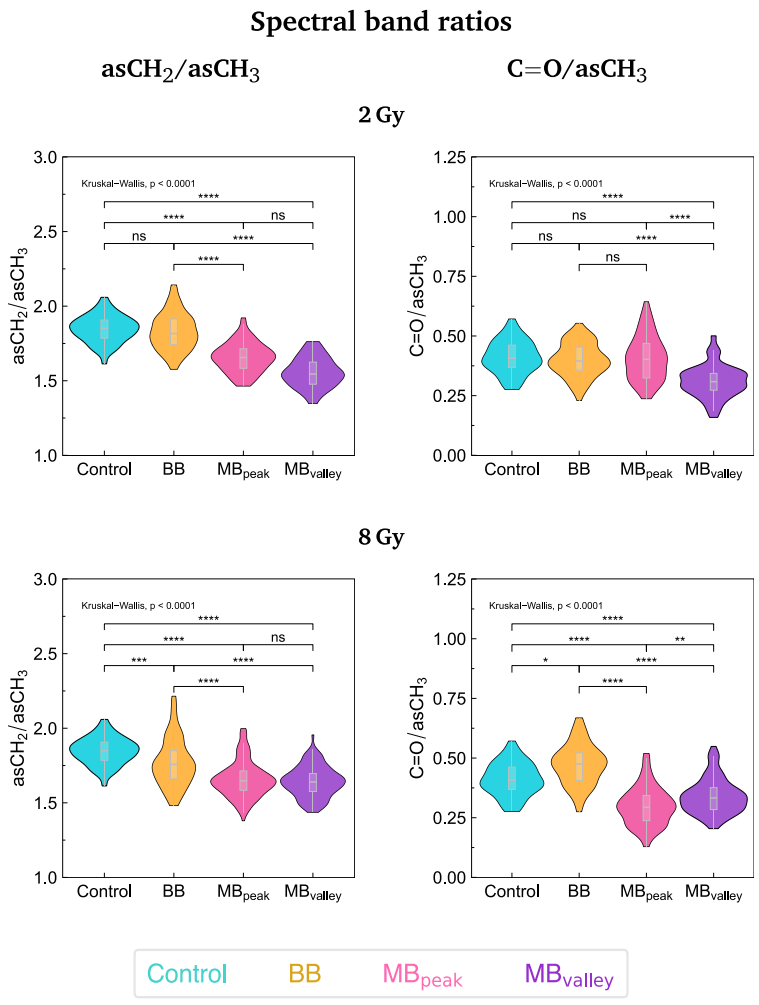

Fig. 8. Violin plots showing the probability density distribution of the $asCH_2/asCH_3$ (first column) and $C{=}O/asCH_3$ (second column) spectral band ratios for LM8 mouse osteosarcoma cells irradiated with 2 Gy (upper row) or 8 Gy (lower row) carbon beams. Colours correspond to the irradiation configurations: blue for Control (non-irradiated), orange for BB, pink for MB_{peak} and purple for MB_{valley}. *p*-value significance levels are indicated as: ns ($p > 0.05$), * ($p \leq 0.05$), ** ($p \leq 0.01$), *** ($p \leq 0.001$), **** ($p \leq 0.0001$).

3.3. Comparison with proton and neon irradiations

PCA results in the A+FP and HW spectral regions for proton and neon irradiations of various tumour cell lines [26,27] are shown in Figs. 9 and 10, respectively. Despite the comparison being performed between different cell lines and doses, data segregation after PCA followed similar trends for the three ion species: irradiated groups are clearly segregated from non-irradiated samples. Moreover, MBRT-treated cells are generally more differentiated from Control groups than BB-irradiated samples. The specific spectral signatures affected by each RT modality are dependent on the type of charged particle. However, some IR signatures common to all three types of ion beams have been identified. In the A+FP regions (Figs. 4 and 9), the peaks in 1670–1666 cm^{-1} (α-helix of AI), 1640–1620 cm^{-1} (β-sheet/unordered structures of AI), 1555–1550 cm^{-1} (α-helix of AII), and 1510–1505 cm^{-1} (β-sheet of AII) are the ones accounting for most of the segregation of MBRT-treated cells from Control and BB-irradiated samples. As discussed in previous sections, alterations of protein-related bands may have been a result of enhanced protein oxidation or cell death mechanisms. Still, each ion species resulted in alterations of specific spectral signatures [26,27]. The fact that protons and heavier ions result in different biological effects is well-known. Therefore, the observed spectral variations among ions may be due to differences in their dose and LET distributions [68].

Regarding lower-frequency spectral bands, the loadings revealed that the heavier the ion species, the greater the relative contribution of the whole FP spectral region (1350–980 cm^{-1}) to data segregation. That is, modifications of nucleic acid- and carbohydrate-related spectral bands seem to be more relevant in data separation for neon irradiations than for proton or carbon irradiations (Figs. 4 and 9) [26,27]. The only common spectral signature to the three ion species that contributed to data segregation was the band at 1240–1220 cm^{-1} (A-form DNA marker of PhI). For the three ions, this band is associated with the separation of Control and BB groups from MBRT-treated cells. Indeed, the appearance in the loadings of further peaks corresponding to the PhII spectral range in neon irradiations suggests more complex DNA alterations than for proton or carbon treatment. Modifications of the PhI and PhII bands are generally associated with an increased number of DNA strand breaks [54], but could also be due to oxidative stress [52] or cell death processes [50].

Fig. 10 shows the PCA in the HW region for protons and neon ions. Comparing with the carbon data (Fig. 7), separation between groups was more pronounced for carbon- and neon-ion beams than for proton irradiations [26,27]. Nonetheless, the methyl bands are generally associated with the segregation of irradiated groups (particularly MBRT-treated cells) from Control samples, whereas alterations of the methylene vibrational modes explain the observed differences between BB and MBRT modalities for the three ion species. Alterations

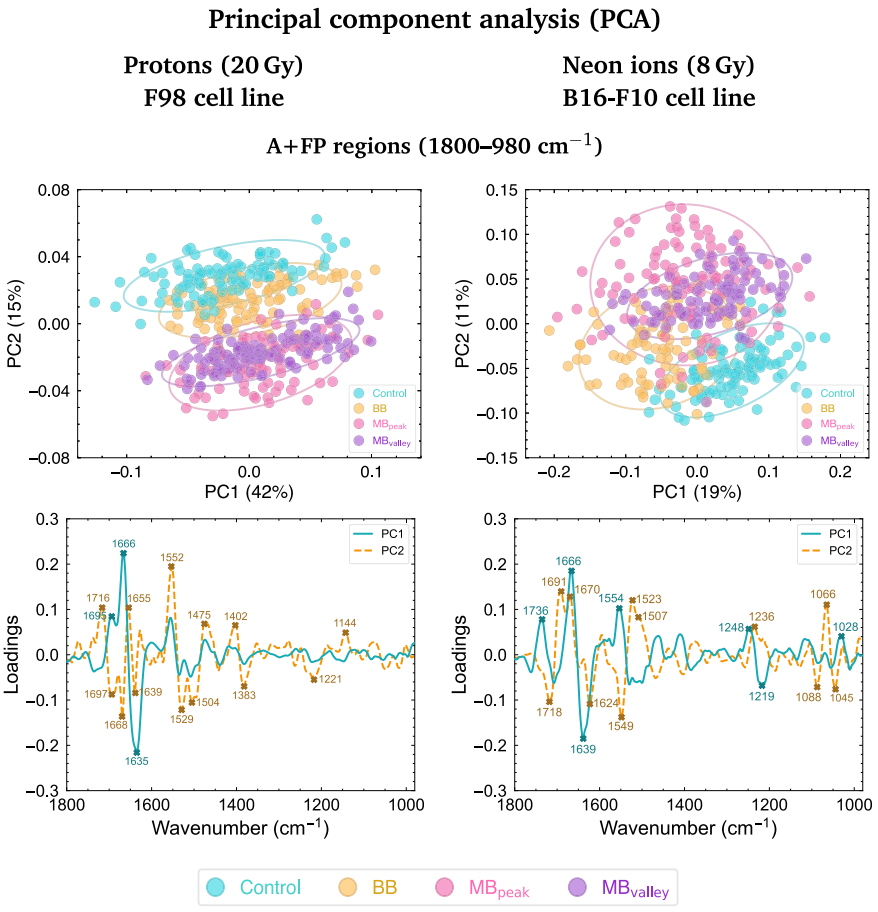

Fig. 9. PCA in the A+FP (1800–980 cm^{-1}) spectral region for proton (left) and neon (right) irradiations. The PC scatter plots (first row) and loadings (second row) are included. Each point on the PC scatter plots represents a cell spectrum, and colours correspond to the irradiation configurations: blue for Control (non-irradiated), orange for BB, pink for MB_{peak} and purple for MB_{valley}. 95% confidence ellipses are included, and explained variances by the PCs are shown in parentheses. In the loadings, the contribution of each spectral band to data separation along PC1 is indicated by solid blue lines, while the bands contributing to the separation along PC2 are indicated by dashed orange lines. The most relevant IR peaks contributing to cluster delineation along PC1 or PC2 are marked with blue or orange labels and crosses, respectively. F98 (rat glioma) or B16-F10 (mouse melanoma) cell lines were subjected to proton or neon irradiations (respectively) in both BB and MBRT conditions; the mean (physical) absorbed doses to samples were 20 Gy (proton beams) or 8 Gy (neon-ion beams).

of these spectral bands, mainly due to MBRT modalities, might result from free radical attacks [63] or cell death processes [54]. In addition, the loadings also show a peak near 1720 cm^{-1} associated with MBRT-treated samples: this spectral signature contributed to the separation of pMBRT and NeMBRT groups from Control and BB-irradiated samples (see PCA in the A+FP regions of Fig. 9). The effects of CMBRT also resulted in modifications of this band, associated with the C=O ester groups. Alterations of this band are considered hallmarks of oxidative stress and cell death [42,52].

Lastly, differences in LET distributions between protons and heavier ions might lead to different biological effects, such as differential protein expression, more clustered DNA breakages or a lower dependence on the oxygen levels to damage cells [11,69]. Thus, the different spectral signatures observed for the three ion species may be a reflection of these distinct radiobiological characteristics. In addition, it should be noted that a variety of cell lines and doses have been used in the proton, carbon and neon MBRT studies [26,27]. Therefore, besides the beam quality, biomolecular differences could arise from the specific characteristics of each cell line and/or be due to the different doses used.

4. Conclusions

In this study, the biomolecular response of the LM8 mouse osteosarcoma cell line to CMBRT was assessed and compared to the effects of conventional carbon RT. The capabilities of SR-FTIRM allowed to investigate subtle differences in the IR signatures of RT-treated samples and correlate them with biomolecular alterations induced by the treatment modalities.

PCA revealed that samples subjected to CMBRT exhibited a clearly different biomolecular pattern from non-irradiated cells and samples exposed to CBB at 24 h post-treatment. In the 1800–980 cm^{-1} spectral region, the main modifications due to CMBRT were indicative of alterations in α-helical and β-sheet secondary structures of proteins. This was consistent with the curve-fitting analysis of the AI band, which revealed an increase in the βU/α spectral ratio for CMBRT-treated cells. These modifications were suggestive of enhanced protein oxidation or cell death mechanisms due to CMBRT. Changes in nucleic acid- and carbohydrate-related IR peaks in the PhI and PhII bands were also mainly induced by CMBRT. CBB-treated samples also underwent important modifications in nucleic acid- and carbohydrate-related spectral bands for the highest dose analysed. The observed alterations in this spectral region could be indicative of DNA and/or RNA backbone conformations and cleavage, DNA degradation or condensation, or oxidative stress. Regarding the 3000–2815 cm^{-1} spectral region, IR spectra of samples subjected to CMBRT were clearly differentiated from Control and CBB groups. CMBRT-induced alterations in the C-H vibrational modes present in this spectral region might be indicative of membrane lipids degradation due to free radical attacks. For 2 Gy irradiations, the effects of the valley regions of CMBRT resulted in the

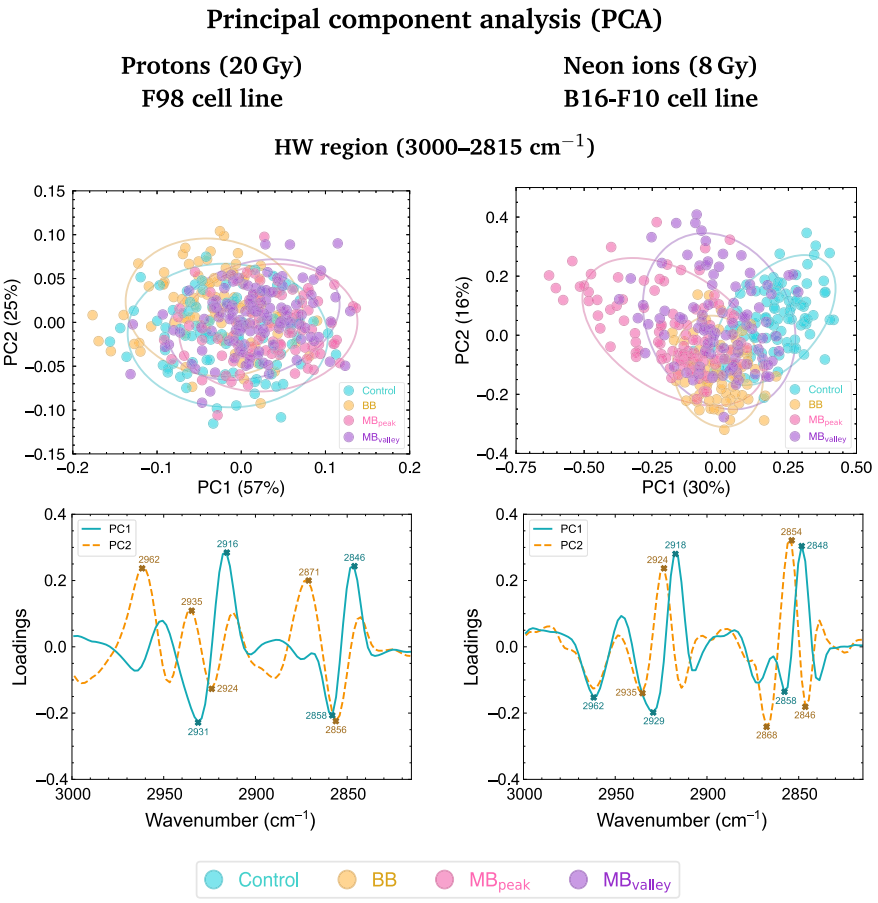

Fig. 10. PCA in the HW (3000–2815 cm^{-1}) spectral region for proton (left) and neon (right) irradiations. The PC scatter plots (first row) and loadings (second row) are included. Each point on the PC scatter plots represents a cell spectrum, and colours correspond to the irradiation configurations: blue for Control (non-irradiated), orange for BB, pink for MB_{peak} and purple for MB_{valley}. 95% confidence ellipses are included, and explained variances by the PCs are shown in parentheses. In the loadings, the contribution of each spectral band to data separation along PC1 is indicated by solid blue lines, while the bands contributing to the separation along PC2 are indicated by dashed orange lines. The most relevant IR peaks contributing to cluster delineation along PC1 or PC2 are marked with blue or orange labels and crosses, respectively. F98 (rat glioma) or B16-F10 (mouse melanoma) cell lines were subjected to proton or neon irradiations (respectively) in both BB and MBRT conditions; the mean (physical) absorbed doses to samples were 20 Gy (proton beams) or 8 Gy (neon-ion beams).

most dissimilar IR signatures from Control cells in the two spectral regions analysed, suggesting a distinct biomolecular effect from that occurring in the CMBRT peak regions. Lastly, comparison of the data of the present study with our results on proton and neon irradiations revealed that MBRT groups were the most dissimilar from Control samples for the three ion species. Each ion species resulted in specific spectral modification but some common spectral signatures contributed to the segregation of MBRT-treated cells from Control and BB groups.

To conclude, this *in vitro* evaluation highlighted the use of synchrotron light to assess the biomolecular impact of a novel oncology treatment approach. Our findings contribute to shed more light on the alterations induced by CMBRT irradiations in the main macromolecules present in cells. Nonetheless, it is important to note that further biological studies will help us to translate the subcellular modifications reported in this analysis into the more complex functional processes involved in tissues.

Main abbreviations and acronyms

A+FP	Amides + Fingerprint
BB	Broad Beam
HW	Higher Wavenumber
IR	Infrared
MBRT	Minibeam Radiation Therapy
PCA	Principal Component Analysis
ROS	Reactive Oxygen Species
RT	Radiation Therapy
SFRT	Spatially Fractionated Radiotherapy
SR-FTIRM	Synchrotron Radiation-based Fourier Transform Infrared Microspectroscopy

CRediT authorship contribution statement

R. González-Vegas: Writing – original draft, Visualization, Software, Investigation, Formal analysis. **M. Cots-Costa:** Formal analysis. **C. Gilbert:** Investigation. **A. Bertho:** Investigation. **O. Seksek:** Methodology. **C. Graeff:** Investigation. **O. Sokol:** Investigation. **W. Tinganelli:** Investigation. **Y. Prezado:** Methodology, Investigation, Funding acquisition, Conceptualization. **I. Yousef:** Writing – review & editing, Supervision, Methodology, Investigation, Funding acquisition, Conceptualization. **I. Martínez-Rovira:** Writing – review & editing, Validation, Supervision, Resources, Project administration, Methodology, Investigation, Funding acquisition, Datacuration, Conceptualization.

Declaration of competing interest

The authors declare that they have no known competing financial interests or personal relationships that could have appeared to influence the work reported in this paper.

Acknowledgements

This study was supported by the Spanish Ministry of Science, Innovation and Universities (grants RYC2018-024043-I, PID2020-114079RA-I00 and PRE2021-097298), by the Catalan Agency for Management of University and Research Grants (2021 SGR 00607), and by the Spanish Association Against Cancer (IDEAS21849MART). This project also received funding from the European Research Council (ERC) under the European Union's Horizon 2020 research and innovation program (Grant Agreement No 817908). Infrared experiments were performed at MIRAS beamline of ALBA Synchrotron Light Source Facility with the collaboration of ALBA staff. Authors would also like to acknowledge the granted beamtime for radiotherapy irradiations at GSI.

Data availability

Research data will be stored and made available in an institutional repository (https://dataverse.csuc.cat/).

References

[1] J. Ferlay, M. Laversanne, M. Ervik, F. Lam, M. Colombet, L. Mery, M. Piñeros, A. Znaor, I. Soerjomataram, F. Bray, Global cancer observatory: Cancer tomorrow (version 1.1), 2024, URL: https://gco.iarc.who.int/tomorrow, (accessed 01 May 2025).

[2] B.A. Lindsey, J.E. Markel, E.S. Kleinerman, Osteosarcoma overview, Rheumatol. Ther. 4 (1) (2016) 25–43, http://dx.doi.org/10.1007/s40744-016-0050-2.

[3] T.F. DeLaney, L. Park, S.I. Goldberg, E.B. Hug, N.J. Liebsch, J.E. Munzenrider, H.D. Suit, Radiotherapy for local control of osteosarcoma, Int. J. Radiat. Oncol. Biol. Phys. 61 (2) (2005) 492–498, http://dx.doi.org/10.1016/j.ijrobp.2004.05.051.

[4] Y. Prezado, Divide and conquer: spatially fractionated radiation therapy, Expert Rev. Mol. Med. 24 (e3) (2022) 1–12, http://dx.doi.org/10.1017/erm.2021.34.

[5] Y. Prezado, M. Dos Santos, W. Gonzalez, G. Jouvion, C. Guardiola, S. Heinrich, D. Labiod, M. Juchaux, L. Jourdain, C. Sebrie, F. Pouzoulet, Transfer of Minibeam Radiation Therapy into a cost-effective equipment for radiobiological studies: a proof of concept, Sci. Rep. 7 (1) (2017) 17295, http://dx.doi.org/10.1038/s41598-017-17543-3.

[6] C. Lamirault, V. Doyère, M. Juchaux, F. Pouzoulet, D. Labiod, R. Dendale, A. Patriarca, C. Nauraye, M. Le Dudal, G. Jouvion, D. Hardy, N.E. Massioui, Y. Prezado, Short and long-term evaluation of the impact of proton minibeam radiation therapy on motor, emotional and cognitive functions, Sci. Rep. 10 (1) (2020) 13511, http://dx.doi.org/10.1038/s41598-020-70371-w.

[7] C. Lamirault, E. Brisebard, A. Patriarca, M. Juchaux, D. Crepin, D. Labiod, F. Pouzoulet, C. Sebrie, L. Jourdain, M. Le Dudal, D. Hardy, L. De Marzi, R. Dendale, G. Jouvion, Y. Prezado, Spatially modulated proton minibeams results in the same increase of lifespan as a uniform target dose coverage in F98-glioma-bearing rats, Radiat. Res. 194 (6) (2020) 715–723, http://dx.doi.org/10.1667/rade-19-00013.1.

[8] M.P. Grams, C.Q. Mateus, M. Mashayekhi, R.W. Mutter, V. Djonov, J.M. Fazzari, H. Xiao, K.M. Frechette, A.J. Wentworth, J.M. Morris, B. Klebel, J.C. Thull, R.M. Guenzel, D.J.S. Wismayer, F. Lucien, S.S. Park, S.C. Lester, Minibeam Radiation Therapy Treatment (MBRT): Commissioning and first clinical implementation, Int. J. Radiat. Oncol. Biol. Phys. 120 (5) (2024) 1423–1434, http://dx.doi.org/10.1016/j.ijrobp.2024.06.035.

[9] I. Martínez-Rovira, Y. Prezado, Minibeam radiation therapy for the management of osteosarcomas: A Monte Carlo study, Med. Phys. 41 (6) (2014) 061706, http://dx.doi.org/10.1118/1.4873693.

[10] I. Martínez-Rovira, W. González, S. Brons, Y. Prezado, Carbon and oxygen minibeam radiation therapy: An experimental dosimetric evaluation, Med. Phys. 44 (8) (2017) 4223–4229, http://dx.doi.org/10.1002/mp.12383.

[11] W. Tinganelli, M. Durante, Carbon ion radiobiology, Cancers 12 (10) (2020) 3022, http://dx.doi.org/10.3390/cancers12103022.

[12] F.A. Dilmanian, A. Rusek, G.R. Fois, J. Olschowka, N.R. Desnoyers, J.Y. Park, I. Dioszegi, B. Dane, R. Wang, D. Tomasi, H. Lee, S.D. Hurley, P.K. Coyle, A.G. Meek, M.K. O'Banion, Interleaved carbon minibeams: An experimental radiosurgery method with clinical potential, Int. J. Radiat. Oncol. Biol. Phys. 84 (2) (2012) 514–519, http://dx.doi.org/10.1016/j.ijrobp.2011.12.025.

[13] A. Bertho, C. Graeff, R. Ortiz, M. Giorgi, C. Schuy, M. Juchaux, C. Gilbert, J. Espenon, J. Oppermann, O. Sokol, W. Tinganelli, Y. Prezado, Carbon minibeam radiation therapy results in tumor growth delay in an osteosarcoma murine model, Sci. Rep. 15 (1) (2025) 7305, http://dx.doi.org/10.1038/s41598-025-91872-6.

[14] J.W. Hopewell, K.-R. Trott, Volume effects in radiobiology as applied to radiotherapy, Radiother. Oncol. 56 (3) (2000) 283–288, http://dx.doi.org/10.1016/s0167-8140(00)00236-x.

[15] A. Bertho, L. Iturri, Y. Prezado, Chapter Two - Radiation-induced immune response in novel radiotherapy approaches FLASH and spatially fractionated radiotherapies, in: C. Mirjolet, L. Galluzzi (Eds.), Ionizing Radiation and the Immune Response - Part A, in: International Review of Cell and Molecular Biology, vol. 376, Academic Press, 2023, pp. 37–68, http://dx.doi.org/10.1016/bs.ircmb.2022.11.005.

[16] S. Sabatasso, J.A. Laissue, R. Hlushchuk, W. Graber, A. Bravin, E. Bräuer-Krisch, S. Corde, H. Blattmann, G. Gruber, V. Djonov, Microbeam radiation-induced tissue damage depends on the stage of vascular maturation, Int. J. Radiat. Oncol. Biol. Phys. 80 (5) (2011) 1522–1532, http://dx.doi.org/10.1016/j.ijrobp.2011.03.018.

[17] A.J. Johnsrud, S.V. Jenkins, R.J. Griffin, General principles of SFRT biology, in: Spatially Fractionated, Microbeam and FLASH Radiation Therapy, in: 2053-2563, IOP Publishing, 2023, pp. 2–1 to 2–18, http://dx.doi.org/10.1088/978-0-7503-4046-5ch2.

[18] R. Dal Bello, T. Becher, M.C. Fuss, M. Krämer, J. Seco, Proposal of a chemical mechanism for mini-beam and micro-beam efficacy, Front. Phys. 8 (2020) 564836, http://dx.doi.org/10.3389/fphy.2020.564836.

[19] E. Lipiec, B.R. Wood, A. Kulik, W.M. Kwiatek, G. Dietler, Nanoscale investigation into the cellular response of glioblastoma cells exposed to protons, Anal. Chem. 90 (12) (2018) 7644–7650, http://dx.doi.org/10.1021/acs.analchem.8b01497.

[20] I. Yousef, O. Seksek, S. Gil, Y. Prezado, J. Sulé-Suso, I. Martínez-Rovira, Study of the biochemical effects induced by X-ray irradiations in combination with gadolinium nanoparticles in F98 glioma cells: first FTIR studies at the Emira laboratory of the SESAME synchrotron, Analyst 141 (7) (2016) 2238–2249, http://dx.doi.org/10.1039/c5an02378e.

[21] I. Martínez-Rovira, O. Seksek, I. Yousef, A synchrotron-based infrared microspectroscopy study on the cellular response induced by gold nanoparticles combined with X-ray irradiations on F98 and U87-MG glioma cell lines, Analyst 144 (21) (2019) 6352–6364, http://dx.doi.org/10.1039/c9an01109a.

[22] I. Martínez-Rovira, O. Seksek, J. Puxeu, J. Gómez, M. Kreuzer, T. Dučić, M.J. Ferreres, M. Artigues, I. Yousef, Synchrotron-based infrared microspectroscopy study on the radiosensitization effects of Gd nanoparticles at megavoltage radiation energies, Analyst 144 (2019) 5511–5520, http://dx.doi.org/10.1039/C9AN00792J.

[23] I. Martínez-Rovira, O. Seksek, I. Dokic, S. Brons, A. Abdollahi, I. Yousef, Study of the intracellular nanoparticle-based radiosensitization mechanisms in F98 glioma cells treated with charged particle therapy through synchrotron-based infrared microspectroscopy, Analyst 145 (6) (2020) 2345–2356, http://dx.doi.org/10.1039/c9an02350j.

[24] M. Sharma, J.C. Crosbie, L. Puskar, P.A.W. Rogers, Microbeam-irradiated tumour tissue possesses a different infrared absorbance profile compared to broad beam and sham-irradiated tissue, Int. J. Radiat. Biol. 89 (2) (2012) 79–87, http://dx.doi.org/10.3109/09553002.2012.721052.

[25] I. Martínez-Rovira, P. Montay-Gruel, B. Petit, R.J. Leavitt, R. González-Vegas, P. Froidevaux, M. Juchaux, Y. Prezado, I. Yousef, M.-C. Vozenin, Infrared microspectroscopy to elucidate the underlying biomolecular mechanisms of FLASH radiotherapy, Radiother. Oncol. 196 (2024) 110238, http://dx.doi.org/10.1016/j.radonc.2024.110238.

[26] R. González-Vegas, I. Yousef, O. Seksek, R. Ortiz, A. Bertho, M. Juchaux, C. Nauraye, L. DeMarzi, A. Patriarca, Y. Prezado, I. Martínez-Rovira, Investigating the biochemical response of proton minibeam radiation therapy by means of synchrotron-based infrared microspectroscopy, Sci. Rep. 14 (1) (2024) 11973, http://dx.doi.org/10.1038/s41598-024-62373-9.

[27] R. González-Vegas, O. Seksek, A. Bertho, J. Bergs, R. Hirayama, T. Inaniwa, N. Matsufuji, T. Shimokawa, Y. Prezado, I. Yousef, I. Martínez-Rovira, Synchrotron-based infrared microspectroscopy unveils the biomolecular response of healthy and tumour cell lines to neon minibeam radiation therapy, Analyst 150 (2) (2025) 342–352, http://dx.doi.org/10.1039/d4an01038h.

[28] T. Asai, T. Ueda, K. Itoh, K. Yoshioka, Y. Aoki, S. Mori, H. Yoshikawa, Establishment and characterization of a murine osteosarcoma cell line (LM8) with high metastatic potential to the lung, Int. J. Cancer 76 (3) (1998) 418–422, http://dx.doi.org/10.1002/(sici)1097-0215(19980504)76:3<418::aid-ijc21>3.0.co;2-5.

[29] M. Lis, W. Newhauser, M. Donetti, M. Durante, U. Weber, B. Zipfel, C. Hartmann-Sauter, M. Wolf, C. Graeff, A facility for the research, development, and translation of advanced technologies for ion-beam therapies, J. Instrum. 16 (03) (2021) T03004, http://dx.doi.org/10.1088/1748-0221/16/03/t03004.

[30] M. Toplak, S.T. Read, C. Sandt, F. Borondics, Quasar: Easy machine learning for biospectroscopy, Cells 10 (9) (2021) 2300, http://dx.doi.org/10.3390/cells10092300.

[31] A. Derenne, T. Claessens, C. Conus, E. Goormaghtigh, Infrared spectroscopy of membrane lipids, in: G.C.K. Roberts (Ed.), Encyclopedia of Biophysics, Springer Berlin Heidelberg, Berlin, Heidelberg, 2013, pp. 1074–1081, http://dx.doi.org/10.1007/978-3-642-16712-6_558.
[32] A. Barth, Infrared spectroscopy of proteins, Biochim. Biophys. Acta (BBA) - Bioenerg. 1767 (9) (2007) 1073–1101, http://dx.doi.org/10.1016/j.bbabio.2007.06.004.
[33] M. Banyay, M. Sarkar, A. Gräslund, A library of IR bands of nucleic acids in solution, Biophys. Chem. 104 (2) (2003) 477–488, http://dx.doi.org/10.1016/s0301-4622(03)00035-8.
[34] H. Ghimire, M. Venkataramani, Z. Bian, Y. Liu, A.G.U. Perera, ATR-FTIR spectral discrimination between normal and tumorous mouse models of lymphoma and melanoma from serum samples, Sci. Rep. 7 (1) (2017) 16993, http://dx.doi.org/10.1038/s41598-017-17027-4.
[35] C. Stani, L. Vaccari, E. Mitri, G. Birarda, FTIR investigation of the secondary structure of type I collagen: New insight into the amide III band, Spectrochim. Acta A 229 (2020) 118006, http://dx.doi.org/10.1016/j.saa.2019.118006.
[36] B.H. Stuart, Infrared Spectroscopy: Fundamentals and Applications, Wiley, 2004, http://dx.doi.org/10.1002/0470011149.
[37] W. André, C. Sandt, P. Dumas, P. Djian, G. Hoffner, Structure of inclusions of Huntington's disease brain revealed by synchrotron infrared microspectroscopy: Polymorphism and relevance to cytotoxicity, Anal. Chem. 85 (7) (2013) 3765–3773, http://dx.doi.org/10.1021/ac400038b.
[38] C. Petibois, G. Déléris, Chemical mapping of tumor progression by FT-IR imaging: towards molecular histopathology, Trends Biotechnol. 24 (10) (2006) 455–462, http://dx.doi.org/10.1016/j.tibtech.2006.08.005.
[39] R Core Team, R: A Language and Environment for Statistical Computing, R Foundation for Statistical Computing, Vienna, Austria, 2023, URL: https://www.R-project.org/.
[40] N. Gault, O. Rigaud, J.-L. Poncy, J.-L. Lefaix, Infrared microspectroscopy study of γ-irradiated and H_2O_2-treated human cells, Int. J. Radiat. Biol. 81 (10) (2005) 767–779, http://dx.doi.org/10.1080/09553000500515368.
[41] F. Gasparri, M. Muzio, Monitoring of apoptosis of HL60 cells by Fourier-transform infrared spectroscopy, Biochem. J. 369 (2) (2003) 239–248, http://dx.doi.org/10.1042/bj20021021.
[42] H.-Y.N. Holman, M.C. Martin, E.A. Blakely, K. Bjornstad, W.R. Mckinney, IR spectroscopic characteristics of cell cycle and cell death probed by synchrotron radiation based Fourier transform IR spectromicroscopy, Biopolymers 57 (6) (2000) 329–335, http://dx.doi.org/10.1002/1097-0282(2000)57:6<329::aid-bip20>3.0.co;2-2.
[43] N. Gault, J.-L. Lefaix, Infrared microspectroscopic characteristics of radiation-induced apoptosis in human lymphocytes, Radiat. Res. 160 (2) (2003) 238–250, http://dx.doi.org/10.1667/rr3020.1.
[44] J.A. Reisz, N. Bansal, J. Qian, W. Zhao, C.M. Furdui, Effects of ionizing radiation on biological molecules—Mechanisms of damage and emerging methods of detection, Antioxid. Redox Signal. 21 (2) (2014) 260–292, http://dx.doi.org/10.1089/ars.2013.5489.
[45] A. Lamberti, C. Sanges, P. Arcari, FT-IR spectromicroscopy of mammalian cell cultures during necrosis and apoptosis induced by drugs, Spectroscopy 24 (5) (2010) 535–546, http://dx.doi.org/10.1155/2010/420791.
[46] U. Zelig, J. Kapelushnik, R. Moreh, S. Mordechai, I. Nathan, Diagnosis of cell death by means of infrared spectroscopy, Biophys. J. 97 (7) (2009) 2107–2114, http://dx.doi.org/10.1016/j.bpj.2009.07.026.
[47] L. Buriankova, Z. Nadova, D. Jancura, M. Refregiers, I. Yousef, J. Mikes, P. Miskovsky, Synchrotron based Fourier-transform infrared microspectroscopy as sensitive technique for the detection of early apoptosis in U-87 MG cells, Laser Phys. Lett. 7 (8) (2010) 613–620, http://dx.doi.org/10.1002/lapl.201010033.
[48] Y. Izumi, K. Fujii, S. Yamamoto, K. Matsuo, H. Namatame, M. Taniguchi, A. Yokoya, DNA damage response induces structural alterations in histone H3–H4, J. Radiat. Res. 58 (1) (2017) 59–65, http://dx.doi.org/10.1093/jrr/rrw086.
[49] J. Yue, Y. Shen, L. Liang, X. Guan, X. Zhang, S. Xu, C. Liang, W. Shi, W. Xu, Tracing the molecular dynamics of living mitochondria under phototherapy via surface-enhanced Raman scattering spectroscopy, Analyst 144 (18) (2019) 5521–5527, http://dx.doi.org/10.1039/c9an01231a.
[50] G. Birarda, D.E. Bedolla, E. Mitri, S. Pacor, G. Grenci, L. Vaccari, Apoptotic pathways of U937 leukemic monocytes investigated by infrared microspectroscopy and flow cytometry, Analyst 139 (12) (2014) 3097–3106, http://dx.doi.org/10.1039/c4an00317a.
[51] E. Lipiec, G. Birarda, J. Kowalska, J. Lekki, L. Vaccari, A. Wiecheć, B. Wood, W. Kwiatek, A new approach to studying the effects of ionising radiation on single cells using FTIR synchrotron microspectroscopy, Radiat. Phys. Chem. 93 (2013) 135–141, http://dx.doi.org/10.1016/j.radphyschem.2013.03.037.
[52] B. Vileno, S. Jeney, A. Sienkiewicz, P. Marcoux, L. Miller, L. Forró, Evidence of lipid peroxidation and protein phosphorylation in cells upon oxidative stress photo-generated by fullerols, Biophys. Chem. 152 (1–3) (2010) 164–169, http://dx.doi.org/10.1016/j.bpc.2010.09.004.
[53] K. Sofińska, N. Wilkosz, M. Szymoński, E. Lipiec, Molecular spectroscopic markers of DNA damage, Molecules 25 (3) (2020) 561, http://dx.doi.org/10.3390/molecules25030561.
[54] E. Lipiec, K.R. Bambery, P. Heraud, C. Hirschmugl, J. Lekki, W.M. Kwiatek, M.J. Tobin, C. Vogel, D. Whelan, B.R. Wood, Synchrotron FTIR shows evidence of DNA damage and lipid accumulation in prostate adenocarcinoma PC-3 cells following proton irradiation, J. Mol. Struct. 1073 (2014) 134–141, http://dx.doi.org/10.1016/j.molstruc.2014.04.056.
[55] K. Sailer, Radiation-induced structural modifications in dsDNA analysed by FT-Raman spectroscopy, Int. J. Radiat. Biol. 69 (5) (1996) 601–613, http://dx.doi.org/10.1080/095530096145616.
[56] M.C. Joiner, B. Marples, P. Lambin, S.C. Short, I. Turesson, Low-dose hypersensitivity: current status and possible mechanisms, Int. J. Radiat. Oncol. Biol. Phys. 49 (2) (2001) 379–389, http://dx.doi.org/10.1016/s0360-3016(00)01471-1.
[57] K. Hauser, Infrared spectroscopy of protein folding, misfolding and aggregation, in: G.C.K. Roberts (Ed.), Encyclopedia of Biophysics, Springer Berlin Heidelberg, Berlin, Heidelberg, 2013, pp. 1089–1095, http://dx.doi.org/10.1007/978-3-642-16712-6_115.
[58] O. Bozkurt-Girit, M.A. Kilic, FTIR spectroscopic characterization reveals short-term macromolecular responses to photobiomodulation in mesenchymal stem cells, Sci. Rep. 15 (1) (2025) 31051, http://dx.doi.org/10.1038/s41598-025-15190-7.
[59] V. Ricciardi, M. Portaccio, L. Manti, M. Lepore, An FTIR microspectroscopy ratiometric approach for monitoring X-ray irradiation effects on SH-SY5Y human neuroblastoma cells, Appl. Sci. 10 (8) (2020) 2974, http://dx.doi.org/10.3390/app10082974.
[60] E. Lipiec, K.R. Bambery, J. Lekki, M.J. Tobin, C. Vogel, D.R. Whelan, B.R. Wood, W.M. Kwiatek, SR-FTIR coupled with principal component analysis shows evidence for the cellular bystander effect, Radiat. Res. 184 (1) (2015) 73–82, http://dx.doi.org/10.1667/rr13798.1.
[61] N.H. Mohd Zainudin, N.N. Talik Sisin, R.A. Rashid, A. Jamil, M.A. Khairil Anuar, K.A. Razak, R. Abdullah, W.N. Rahman, Cellular analysis on the radiation induced bystander effects due to bismuth oxide nanoparticles with 6 MV photon beam radiotherapy, J. Radiat. Res. Appl. Sci. 15 (3) (2022) 318–325, http://dx.doi.org/10.1016/j.jrras.2022.08.003.
[62] C. Slattery, K. Nguyen, L. Shields, I. Vega-Carrascal, S. Singleton, F.M. Lyng, B. McClean, A.D. Meade, Application of advanced non-linear spectral decomposition and regression methods for spectroscopic analysis of targeted and non-targeted irradiation effects in an in-vitro model, Int. J. Mol. Sci. 23 (21) (2022) 12986, http://dx.doi.org/10.3390/ijms232112986.
[63] C. Petibois, G. Déléris, Oxidative stress effects on erythrocytes determined by FT-IR spectrometry, Analyst 129 (10) (2004) 912–916, http://dx.doi.org/10.1039/b408931f.
[64] T.A.M. Masilela, Y. Prezado, Monte Carlo study of the free radical yields in minibeam radiation therapy, Med. Phys. 50 (8) (2023) 5115–5134, http://dx.doi.org/10.1002/mp.16475.
[65] R. Kinder, C. Ziegler, J.M. Wessels, Gamma-Irradiation and UV-C light-induced lipid peroxidation: a Fourier transform-infrared absorption spectroscopic study, Int. J. Radiat. Biol. 71 (5) (1997) 561–571, http://dx.doi.org/10.1080/095530097143897, PMID: 9191901.
[66] A. Oleszko, S. Olsztyńska-Janus, T. Walski, K. Grzeszczuk-Kuć, J. Bujok, K. Gałecka, A. Czerski, W. Witkiewicz, M. Komorowska, Application of FTIR-ATR spectroscopy to determine the extent of lipid peroxidation in plasma during haemodialysis, BioMed Res. Int. 2015 (2015) 1–8, http://dx.doi.org/10.1155/2015/245607.
[67] A. Gianoncelli, L. Vaccari, G. Kourousias, D. Cassese, D.E. Bedolla, S. Kenig, P. Storici, M. Lazzarino, M. Kiskinova, Soft X-Ray microscopy radiation damage on fixed cells investigated with synchrotron radiation FTIR microscopy, Sci. Rep. 5 (1) (2015) 10250, http://dx.doi.org/10.1038/srep10250.
[68] F. Tommasino, E. Scifoni, M. Durante, New ions for therapy, Int. J. Part. Ther. 2 (3) (2016) 428–438, http://dx.doi.org/10.14338/ijpt-15-00027.1.
[69] M. Winter, I. Dokic, J. Schlegel, U. Warnken, J. Debus, A. Abdollahi, M. Schnölzer, Deciphering the acute cellular phosphoproteome response to irradiation with X-rays, protons and carbon ions, Mol. Cell. Proteom. 16 (5) (2017) 855–872, http://dx.doi.org/10.1074/mcp.m116.066597.